Discovering minimum energy pathways via distortion symmetry groups

Jason M. Munro, Hirofumi Akamatsu, Haricharan Padmanabhan, Vincent S. Liu, Yin Shi, Long-Qing Chen, Brian K. VanLeeuwen, Ismaila Dabo, and Venkatraman Gopalan

Discovering minimum energy pathways via distortion symmetry groups

Jason M. Munro,[1, 2, *] Hirofumi Akamatsu,[3] Haricharan Padmanabhan,[1] Vincent S. Liu,[1] Yin Shi,[1] Long-Qing Chen,[1] Brian K. VanLeeuwen,[4] Ismaila Dabo,[1, 2] and Venkatraman Gopalan[1, 5, 6]

[1]*Department of Materials Science and Engineering and Materials Research Institute,*
The Pennsylvania State University, University Park, PA 16802, USA
[2]*Penn State Institutes of Energy and the Environment,*
The Pennsylvania State University, University Park, PA 16802, USA
[3]*Department of Applied Chemistry, Kyushu University, Fukuoka 819-0395, Japan*
[4]*Two Sigma Investments, New York, New York 10013, USA*
[5]*Department of Physics, The Pennsylvania State University, University Park, Pennsylvania 16802, USA*
[6]*Department of Engineering Science and Mechanics,*
The Pennsylvania State University, University Park, Pennsylvania 16802, USA

Physical systems evolve from one state to another along paths of least energy barrier. Without *a priori* knowledge of the energy landscape, multidimensional search methods aim to find such minimum energy pathways between the initial and final states of a kinetic process. However in many cases, the user has to repeatedly provide initial guess paths, thus ensuring that the reliability of the final result is heavily user-dependent. Recently, the idea of "distortion symmetry groups" as a complete description of the symmetry of a path has been introduced. Through this, a new framework is enabled that provides a powerful means of classifying the infinite collection of possible pathways into a finite number of symmetry equivalent subsets, and then exploring each of these subsets systematically using rigorous group theoretical methods. The method, which we name the distortion symmetry method (DSM), is shown to lead to the discovery of new, previously hidden pathways for the case studies of bulk ferroelectric switching and domain wall motion in proper and improper ferroelectrics, as well as in multiferroic switching. These provide novel physical insights into the nucleation of switching pathways at experimentally observed domain walls in $Ca_3Ti_2O_7$, as well as how polarization switching can proceed without reversing magnetization in $BiFeO_3$. Furthermore, we demonstrate how symmetry-breaking from a highly symmetric pathway can be used to probe the non-Ising (Bloch and Néel) polarization components integral to transient states involved in switching in $PbTiO_3$. The distortion symmetry method is applicable to a wide variety of physical phenomena ranging from structural, electronic and magnetic distortions, diffusion, and phase transitions in materials.

I. INTRODUCTION

Minimum energy paths (MEPs)[1] are of utmost importance in physical sciences where they are used to study any arbitrary distortion in a material, such as changes in molecular confirmations and chemical reactions[2–4], structural or electronic phase transitions[5–7], diffusion[4,8,9], ferroelectric and magnetic switching[10–14], surface reconstructions and the motion of interfaces such as dislocations[15,16] and domain walls[17,18]. All of these processes require knowledge of the underlying atomic motion provided by the MEPs. Finding MEPs can however be difficult due to the lack of *a priori* knowledge of the potential energy landscape, given the prohibitive computational cost in determining it for processes involving a large number of atoms. The goal is then, given a starting and ending point in the landscape, to find the path connecting them that provides the lowest energy barrier, such that the forces perpendicular to the path are at a minimum; this defines an MEP.

Among chain-of-states methods for determining MEPs[19], a commonly used approach is with nudged elastic band (NEB) calculations[20]. However, the application of this method raises a major difficulty; the relaxed path depends necessarily on the initial conditions, and repeated multiple starting points are required to explore additional pathways that may exist along the potential energy surface. Traditionally, this initialization is performed stochastically, or by altering one or several images to construct new paths via physical intuition or geometry optimization[21–24]. While this is effective in many situations given sufficient computational attempts, it does not treat the path as a singular unit, and as will be shown, can lead to the omission of lower energy paths. Further, this approach cannot ensure that the path found is indeed the one of lowest energy.

These limitations of the NEB algorithm have recently been formally described by VanLeeuwen and Gopalan, using the language of symmetry[25]. They show that the symmetry of a distortion pathway in a material is entirely described by one of the 17,803 double antisymmetry space groups[26], and that this symmetry is only conserved or raised by the NEB algorithm, but never lowered. It is this fundamental fact that restricts access to MEPs with lower path symmetry without a symmetry-breaking perturbation of the initial path. In contrast to stochastic methods of breaking path symmetry in which only one or a few intermediate images are perturbed, as is currently practiced, group theory offers a systematic way to perturb an entire path (including all the images) using modes obtained from irreducible representations (irreps). By perturbing with these modes, the symmetry
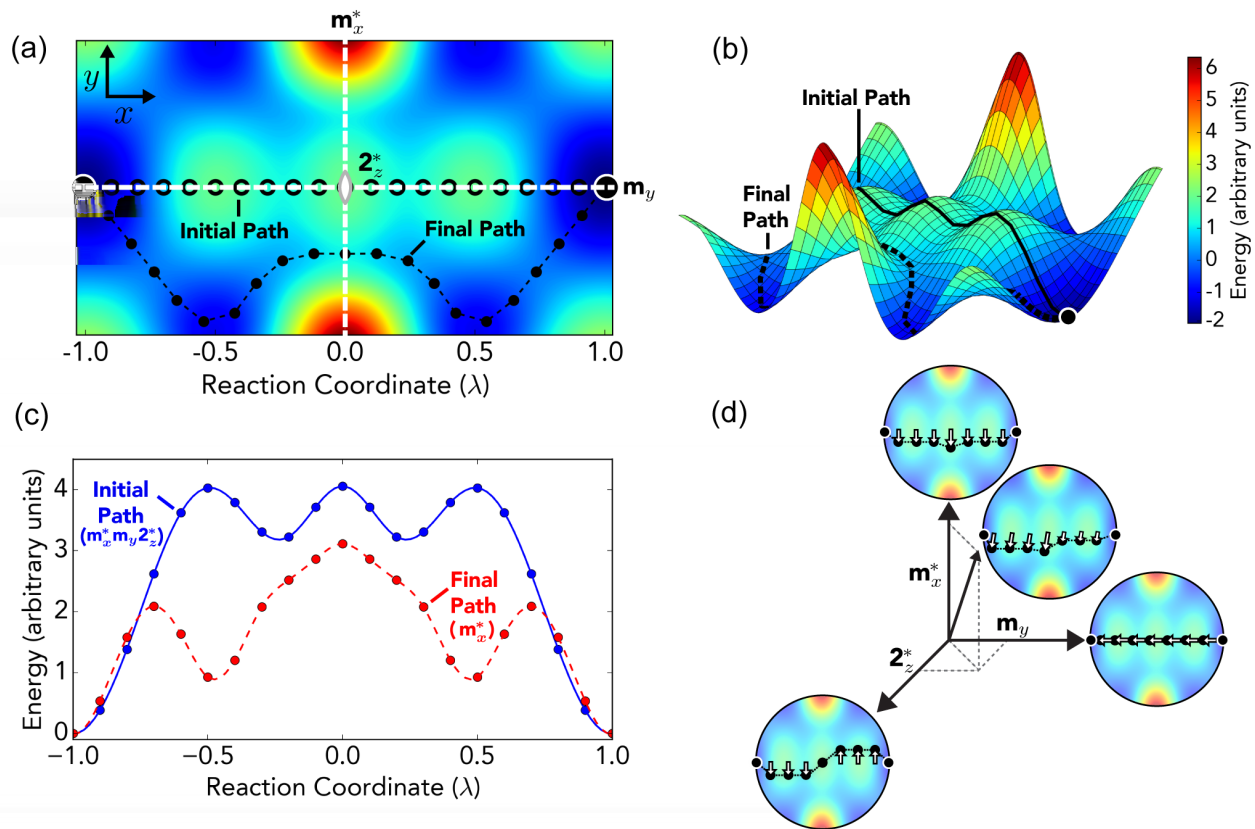
FIG. 1. Illustration of distortion symmetry and path perturbation. (a) & (b) The potential energy landscape and images of atoms representing atomic motion on the surface of a material. The initial linear path has a path symmetry of $m_x^* m_y^* 2_z^*$. Perturbing the initial path with the symmetry-adapted perturbation associated with the Γ_2 irrep brings the path down to m_x^* symmetry, and produces the lowest energy path once an NEB calculation is run. Both the initial linear path and the final relaxed path resulting from the NEB algorithm are shown. (c) The energy relative to the initial and final state as a function of reaction coordinate for both the high (initial) and low energy paths. (d) The symmetry adapted components projected out of an arbitrary perturbation to the initial path. The mode shown along the axis is used to perturb the initial high-energy path.

of the path can then be systematically lowered. This symmetry-based approach which we call the *distortion symmetry method* (DSM) thus provides a more comprehensive and efficient stepwise procedure for classifying all of the infinite paths into a finite number of symmetry equivalent subsets, and then exploring each of these using group theoretical tools.

To motivate the need for symmetry-adapted perturbations, consider the potential energy landscape shown in Figures 1(a) and 1(b) to which we apply the DSM. (For the sake of illustration, the landscape here is given *a priori*, but the conclusions of the analysis are general.) If this system is taken to represent the motion of an atom on the surface of a material, a symmetry analysis of the path can be performed using only the information provided by the potential energy landscape. In this example, the reaction coordinate, λ, is naturally taken as the horizontal coordinate which varies between the two states, renormalized from -1 (the initial state) to $+1$ (the final state). To describe path symmetry, a new antisymmetry

operation called distortion reversal symmetry (1^*) was introduced by VanLeeuwen and Gopalan[25].

Distortion symmetry groups are the product of conventional spatial symmetry groups and the distortion reversal operation 1^*. A distortion can be described by a set of atomic positions written as $\vec{r'}_i = \vec{r}_i + \lambda \vec{d}_i$, where $\vec{r'}_i$ and $\vec{r}_i$ are the final and initial positions of atom i, λ is the reaction coordinate varying between $\lambda = -1$ and $\lambda = +1$, and $\vec{d}_i$ is the displacement vector for atom i (see Figure 2). The 1^* operation reverses the distortion as follows: $1^*(\lambda) = -\lambda$. In order to find the distortion symmetry group of of a path, the following procedure can be employed: First, the intersection group (H) of the conventional spatial symmetry operations of all the images in a path is obtained. Then possible "starred" operations (A^*) that map the structure at the reaction coordinate λ to the ones at $-\lambda$ are identified. These operations can then be written as $A^* = A1^*$, where A would be a symmetry operation of the structure at $\lambda = 0$. The distortion group can then be obtained as $H \cup A^* H$.

Taking the initial path as the linear interpolation of images between the two end points, the resulting distortion symmetry is $m_x^* m_y 2_z^*$. The notation m_y for example represents a mirror perpendicular to the y-axis, and 2_z represents a 2-fold rotation axis parallel to the z-axis as shown in Figure 1. The three non-trivial operations in this group are m_x^*, m_y, and 2_z^*, which leave the initial path shown in Figure 1 invariant when applied to all of the images that compose it. Operations marked with an asterisk that are referred to as "starred" operations can be physically interpreted as conventional spatial operations that also require reversing the direction of the path in order to leave it invariant. It should be noted that the DSM described in this paper can always be applied, irrespective of whether starred symmetry operations are present or not. Furthermore, even if the MEP lacks any significant symmetry, it is sometimes possible to construct a highly symmetrized initial starting path that allows us to discover the MEP using the proposed group theoretical methods.

Running an NEB calculation on the initial linear path with distortion group $m_x^* m_y 2_z^*$ produces the energy profile shown in blue in Figure 1(c). However, in this example, an alternate path with a lower energy barrier exists that is initially inaccessible due to the balanced forces arising from path symmetry conservation in the NEB algorithm. To obtain this lower energy path, the initial linear path needs to be perturbed. Group theory shows that any arbitrary perturbation of this initial path can be decomposed into a linear combination of *exactly* three non-trivial symmetry-adapted perturbative components (Figure 1(d)) that transform as the three irreps, Γ_2, Γ_3, and Γ_4 shown in Supplementary Table 1[27]. These three irreps have kernel symmetry groups of m_x^*, m_y, and 2_z^* respectively. Modifying the initial path with symmetry lowering perturbations such that the new path transforms as one of these kernel symmetry groups, results in three new initial paths that conserve only these symmetries. The new initial path with m_y symmetry simply returns to the original linearly interpolated path once the NEB algorithm is employed. It is only the m_x^* and 2_z^* perturbations that produce new paths after NEB optimization, with only the m_x^* path providing a path with a lower overall energy barrier. Thus, the MEP in this example has a path symmetry group of m_x^*.

It should be noted that there are additional methods commonly employed to try and obtain MEPs that are not of the chain-of-states type mentioned. In general, these can be categorized into two types: those involving potential energy "surface-walking"[21,22,28], and others involving Monte Carlo sampling[29–33]. In walking algorithms, such as those based on restricted-step Newton Raphson methods[34–36], saddle points are searched for by starting with a reference structure which sits in a local minima, and then moving it within the potential energy landscape according to a system dependent reaction coordinate. Often, this is chosen through gradient and Hessian information. It should also be mentioned that these kinds of system specific reaction coordinates can be used to generate starting paths for chain-of-states approaches such as the NEB method. A recent example of this includes the Normal-Mode Transition Approximation[37], which aims to construct approximate pathways of reactions that can be used as starting paths for NEB calculations through reaction coordinates obtained via phonon mode calculations. For many techniques involving a sampling procedure such as transition[30–32] and discrete path[38,39] sampling, and minima hopping guided pathway searching[33], a Monte Carlo sampling procedure for structures or paths is performed in conjunction with other calculations such as those involving molecular dynamics or geometry optimization.

Using the distortion symmetry method (DSM) described in this study has significant advantages compared to many of these other methods. Firstly, the intrinsic advantages of the NEB algorithm are able to be effectively utilized. These include robustness and a relatively reasonable computational cost which allow for the accommodation of large material systems. Furthermore, the calculated path perturbations used to break the conserved symmetries and induce instabilities only take up to tens of seconds of CPU time on a single core for systems similar in size to the examples shown in this study. Although other methods involving surface-walking or path sampling may be able to reproduce paths obtained by this method, costly calculations associated with obtaining Hessian information, or running many first-principles molecular dynamics or geometry optimization calculations are completely avoided.

Next, we illustrate the power of the DSM using three examples of ferroelectric polarization switching, two involving bulk switching, and one involving a domain wall motion. Understanding the minimum energy pathway for polarization reversal is of practical interest to a broad range of technologies such as optical communications, ultrasound imaging and sensing, precision actuation, infrared imaging and nonvolatile memory. While bulk ferroelectric switching provides a simplistic picture of the polarization reversal process that often involves defects and grain boundaries, it is computationally less intensive, and still provides important insights into the atomic behavior in an ideal lattice. Further, the symmetry method described below can also be used for larger molecular dynamics simulations of domain wall motion using symmetrized supercells[40].

II. METHODS

Nudged elastic band (NEB) calculations[20] were used in this study. The Vienna Ab initio Simulation Package[41–44] was used for all structural optimization and NEB calculations. The ability to generate symmetry adapted perturbations was implemented into a standalone piece of Python code and the open-source Quantum-ESPRESSO[45] software package. This is dis-
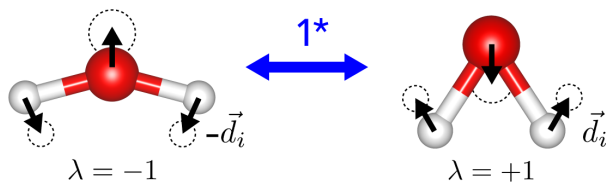
FIG. 2. Distortion of a water molecule described by atomic displacement vectors $\vec{d_i}$. Applying the 1^* operation reverses the distortion by reversing the individual displacements of the atoms. By parameterizing the distortion with a reaction coordinate λ that varies between $\lambda = -1$ and $\lambda = +1$, we can write: $1^*(\lambda) = -\lambda$.

cussed in more detail in the implementation section of the supplementary material. VESTA[46] was used for the visualization of all of the structures.

To generate the symmetry-adapted perturbations, a random perturbation to the path was first generated. Then, projection operators[47] were constructed using the matrix representations of the elements in the path's distortion group, as well as the matrices of its physically irreducible representations. The former was obtained using the SPGLIB[48] library, and the latter with the listing by Stokes and coworkers[49]. The operators were then applied to a vector representing the arbitrary path perturbation to project out its symmetry-adapted components. The projection operators are defined as follows:

$$\hat{P}_{kk}^{\Gamma_n} = \frac{l_n}{h} \sum_R \left[D_{kk}^{\Gamma_n}(R) \right]^* \hat{R} \qquad (1)$$

Where l_n is the dimension of the irrep Γ_n, h is the order of the distortion group, $\hat{R}$ is a symmetry operation from the distortion group, and $D_{kk}^{\Gamma_n}(R)$ is the kth diagonal matrix entry of the matrix representation of element R in the physically irreducible representation Γ_n. For irreps of dimension greater than one, multiple perturbative modes are obtained for each $k = 1, ..., l_n$. These form a representation space, where their linear combination is taken to produce the final perturbation.

A. Ca₃Ti₂O₇ calculations

A $Z = 4$ orthorhombic cell was used for the initial and final states. All first-principles calculations, including initial structural optimizations of the NEB end-points, were completed using the revised Perdew-Burke-Ernzerhof generalized-gradient approximation functional[50] (PBEsol) that has been shown to improve properties of densely-packed solids, and has been used effectively with $Ca_3Ti_2O_7$[14,51]. A 6x6x2 k-point mesh, 600 eV plane-wave cutoff, and 1×10^{-4} eV energy error threshold were used. The projector augmented wave method was used to represent the ionic cores. There were 10 electrons for Ca $(3s^23p^64s^2)$, 12 electrons for Ti

$(3s^23p^64s^23d^2)$, and 6 electrons for O $(2s^22p^4)$ treated explicitly. The Methfessel-Paxton smearing scheme[52] was used with a smearing width of 0.2 eV. NEB calculations were run using the G-SSNEB algorithm[53], until forces were below 0.02 eV Å^{-1}. The path perturbations were normalized such that the maximum displacement of any one atom was set to 0.1 Å.

B. BiFeO₃ calculations

A $Z = 8$ pseudocubic cell was used for the initial and final states (Supplementary Figure 2[27]). All first-principles calculations, including initial structural optimizations of the NEB end-points, were completed with the GGA+U approximation[54,55] to density-functional theory which has been used effectively with $BiFeO_3$[13,56,57]. A $U_{eff} = 4$ eV value was used to better treat the 3d electrons in Fe which has previously been benchmarked and utilized[13,58,59]. Repeating the calculations after altering the U_{eff} value by 1 eV only changed the magnitude of the net magnetization, and did not alter the direction. This can be seen in magnetization data for $U_{eff} = 3$ eV in Supplementary Figure 6[27]. A 4x4x4 k-point mesh, 500 eV plane-wave cutoff, and 1×10^{-6} eV energy error threshold were used for the NEB calculations. The same parameters were used for the magnetization calculations, but with a slightly smaller energy error threshold of 1×10^{-7} eV. The projector augmented wave method was used to represent the ionic cores. There were 15 electrons for Bi $(5d^{10}6s^26p^3)$, 14 electrons for Fe $(3p^63d^64s^2)$, and 6 electrons for O $(2s^22p^4)$ treated explicitly. The tetrahedron smearing scheme with Blöchl corrections[60] was used with a smearing width of 0.05 eV. NEB calculations were run using the G-SSNEB algorithm[53], until forces were below 0.02 eV Å^{-1}. The path perturbations were normalized such that the maximum displacement of any one atom was set to 0.1 Å.

C. PbTiO₃ calculations

All first-principles calculations, including initial structural optimizations of the NEB end-points, were completed using the revised Perdew-Burke-Ernzerhof generalized-gradient approximation functional[50] (PBEsol) that has been shown to improve properties of densely-packed solids, and has been used effectively with $PbTiO_3$[61]. A 1x6x6 k-point mesh, 400 eV plane-wave cutoff, and 1×10^{-7} eV energy error threshold were used. The projector augmented wave method was used to represent the ionic cores. There were 4 electrons for Pb $(6s^26p^2)$, 4 electrons for Ti $(3d^34s^1)$, and 6 electrons for O $(2s^22p^4)$ treated explicitly. The Gaussian smearing scheme was used with a smearing width of 0.01 eV. NEB calculations were run using the regular

NEB algorithm, until forces were below $0.01\,\mathrm{eV\,\mathring{A}^{-1}}$. The path perturbations were normalized such that the maximum displacement of any one atom was set to $0.1\,\mathring{A}$.

III. RESULTS AND DISCUSSION

A. Application to domain switching in improper ferroelectric $Ca_3Ti_2O_7$

The first example involves the bulk switching of a recently discovered ferroelectric crystal $Ca_3Ti_2O_7$. This example illustrates how the commonly employed method of altering the initial path through physical considerations of the kinetic process may fail to discover hidden MEPs, especially when the images altered are shared by the new MEP. The example will also illustrate how to systematically explore distortions of the initial path constructed with both $k = (0,0,0)$ and $k \neq (0,0,0)$ irreps using group theory, where k indicates a reciprocal lattice vector in the first Brillouin zone.

Inversion symmetry breaking in $Ca_3Ti_2O_7$ arises from a trilinear coupling between a polar mode and two other oxygen octahedral rotation modes that transform as the X_{3-} and X_{2+} irreps of the high symmetry $I4/mmm$ structure[62]. Nowadnick and Fennie[14] employed various group theory methods in conjunction with physical intuition supported by density-functional theory (DFT) calculations to identify the switching pathway between a polarization "up" and a polarization "down" state, each with a structural symmetry of $Cmc2_1$ (see Figure 3(a)). These were obtained by reversing the X_{2+} mode associated with octahedral rotations about the z-axis. Three low energy paths were identified that pass through intermediate structures of $Pnma$, $Pbcn$, and $C2/c$ symmetry.

The DSM can be applied to this problem with significant results. First, a linearly interpolated path is constructed with a distortion symmetry of $Cmcm^*$ that passes through a high-symmetry paraelectric structure $Cmcm$. Using the NEB algorithm, the high-energy profile shown in blue in Figure 3(b) is revealed. From here, path perturbations are constructed using the non-trivial irreps of the group $Cmcm^*$ at the Γ point $k = (0,0,0)$, and at the high symmetry Y point $k = (1,0,0)$ (Supplementary Table 2[27]). This latter point was chosen for this particular example, as the isotropy subgroups of the irreps appear to match the distortion groups of the previously reported low energy two-step paths (Figure 3(b)). In general, this knowledge would not be present, and perturbations would be generated and applied using irreps at all high symmetry k-points of the distortion group. It is important to note that perturbations constructed with these require a sufficiently large supercell in order to accommodate a loss of translational symmetry. After applying the perturbations, NEB calculations are run with three paths of lower energy being produced from the initial paths associated with irreps Y_{4+}, Y_{2-}, and Γ_{4+}.

These have Pn^*ma, $Pbcn^*$, and $C2^*/c$ (Figure 3(c)) symmetry respectively, and match the low energy two-step paths reported by Nowadnick and Fennie[14]. The curves fitted to much of the data in this study, such as those in Figure 3(b), have been made symmetric about $\lambda = 0$ when the paths contains "starred" symmetry. The asymmetries that are present in the data itself are as a result of numerical errors, which can commonly be seen in many reported MEPs (see Supplementary Table 1 in Ref. 25).

With previously reported paths having been recreated, further perturbations can be generated using the irreps of their distortion groups ($Pbcn^*$, Pn^*ma, and $C2^*/c$). These are then applied to each respective path, and new NEB calculations are run, resulting in six new four-step paths of lower energy that were not previously reported. Paths obtained from the $Pbcn^*$ and Pn^*ma two-step paths have very similar barriers, with the $P2_1^*/c$ and $Pn^*a2_1^*$ paths from perturbation of the Pn^*ma being slightly lower ($22\,\mathrm{meV/Ti}$) as illustrated in Figure 3(b). The four-step paths obtained from $C2^*/c$ are lower in energy than the two-step parent, but have barriers similar in energy to the two-step $Pbcn^*$ and Pn^*ma paths.

The six new four-step paths obtained have similar character, with each pair of paths passing through the same structure at $\lambda = 0$ as the two-step path they are from. For paths obtained from the Pn^*ma, $Pbcn^*$, and $C2^*/c$ paths, these structures are $Pnma$, $Pbcn$, and $C2/c$ respectively, as shown in Figure 4(a). Figure 4 also displays snapshots of the $Ca_3Ti_2O_7$ supercell for one of the four-step paths from each pair, as well as plots of displacive mode amplitudes as a function of reaction coordinate. These are obtained by decomposing the distorted structures along each the paths into modes of atomic displacements that transform as the irreps of the high-symmetry parent structure with $I4/mmm$ symmetry[63].

In all of the two-step paths, the switching process involves the simultaneous rotation of two pairs of oxygen octahedra in each step. For the Pn^*ma path, both pairs are within one of the perovskite layers of the structure, and for the $Pbcn^*$ and $C2^*/c$ paths, there is one pair in each layer. In all of the four-step paths, each step instead consists of the simultaneous rotation of a single pair of octahedra in one of the layers, with the difference between all six paths being the order of the transition of all four pairs in the unit cell. This is illustrated with the snapshots in Figure 4a, as well as the plotted mode amplitudes in Figure 4b. For all four-step-paths, the distorted structures at $\lambda = -0.5$ and $\lambda = 0.5$ show non-zero amplitudes of similar magnitude for displacive modes that transform as the Γ_{5+}, M_{5+}, M_{5-}, X_{1-}, and X_{2+} irreps of $I4/mmm$. The paths then involve two of these increasing in magnitude, and three decreasing to zero at $\lambda = 0$. It is different combinations of these two sets of increasing and decreasing modes that produce the $Pnma$, $Pbcn$, and $C2/c$ transition structures.

The prediction and experimental observation of a variety of polar domains in $Ca_3Ti_2O_7$ points to the existence of 180° domain walls with a local antipolar $Pnma$
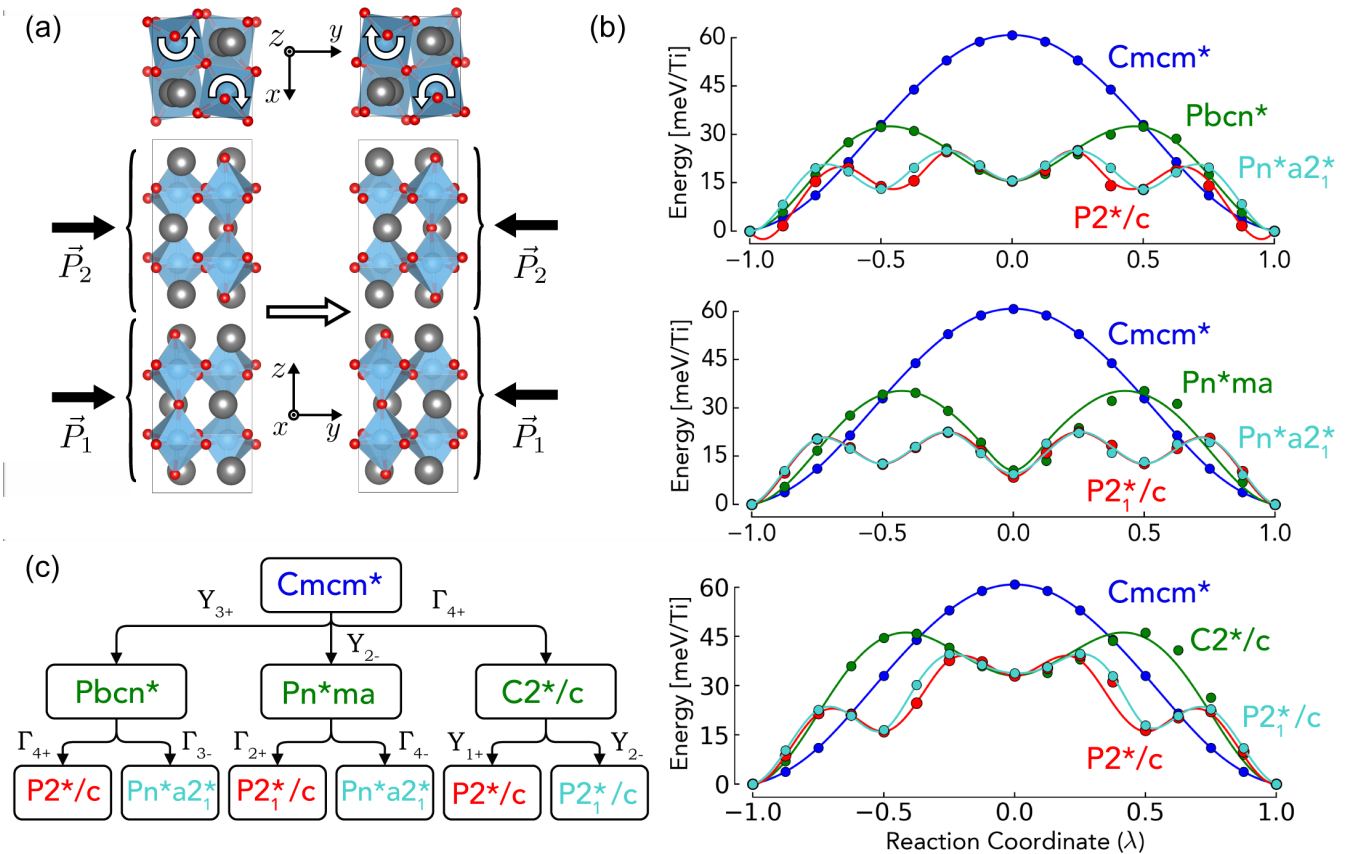
FIG. 3. Ferroelectric switching pathways in $Ca_3Ti_2O_7$ obtained with the symmetry-based method. (a) The initial and final states of bulk polarization switching in the $Ca_3Ti_2O_7$ Ruddlesden-Popper ($n = 2$) structure. Arrows indicating the direction of the octahedral rotations in the z-direction are shown, as well as the polarization vectors for each of the perovskite slabs. Ca, Ti, and O are indicated by the grey, blue, and red atoms respectively. (b) The energy relative to the initial and final state as a function of reaction coordinate for both the two-step and four-step paths from the NEB method. The upper plot corresponds to perturbations illustrated by the left half of the tree in panel c, and the bottom with the right half. (c) Tree of distortion symmetry groups of resulting paths after perturbation.

structure[14,64,65]. Pathways that pass through this $Pnma$ structure, such as the four-step paths with $Pn^*a2_1^*$ and $P2_1^*/c$ symmetry obtained from perturbing the Pn^*ma path, characterize switching at this interface. However, the nucleation of other previously reported switching pathways with similarly low energy barriers that pass through $Pbcn$ and $C2/c$ structures has not been clear. The new four-step paths reported might also provide insight into this problem due to the commonalities between them – each of the steps in all of the pathways involve the rotation of a single pair of oxygen octahedra in one of the perovskite layers of the structure. Consequently, the switching process may begin with a single pair of octahedra transitioning at the antipolar wall, with $Pnma$, $Pbcn$, and $C2/c$ structures at the $\lambda = 0$ point of the pathway enabled by the specific order in which other pairs transition. Further study on how this order could be selectively controlled may be of interest as the presence of specific ferroelectric switching pathways can be dependent on many factors including local stress, domain size,

and applied electric field. Furthermore, this selective control of specific ferroelectric switching pathways being recently demonstrated experimentally[66,67]. It should be noted that strain specifically may be able to play a role as the $Pbcn$ structure of $Ca_3Ti_2O_7$ has recently been stabilized theoretically using epitaxial strain[68]. Overall, this practical example illustrates the importance of the holistic treatment of NEB paths and their perturbations. By only considering different paths defined by alteration of the original transition image at $\lambda = 0$, additional lower energy paths may be missed such as in this example.

B. Application to multiferroic switching in $BiFeO_3$

The second example of the DSM involves a well-studied multiferroic, $BiFeO_3$, and illustrates how distortion symmetry can help access and manipulate functional properties of materials such as coupling of polarization and magnetization. $BiFeO_3$ is of interest for its well-known room
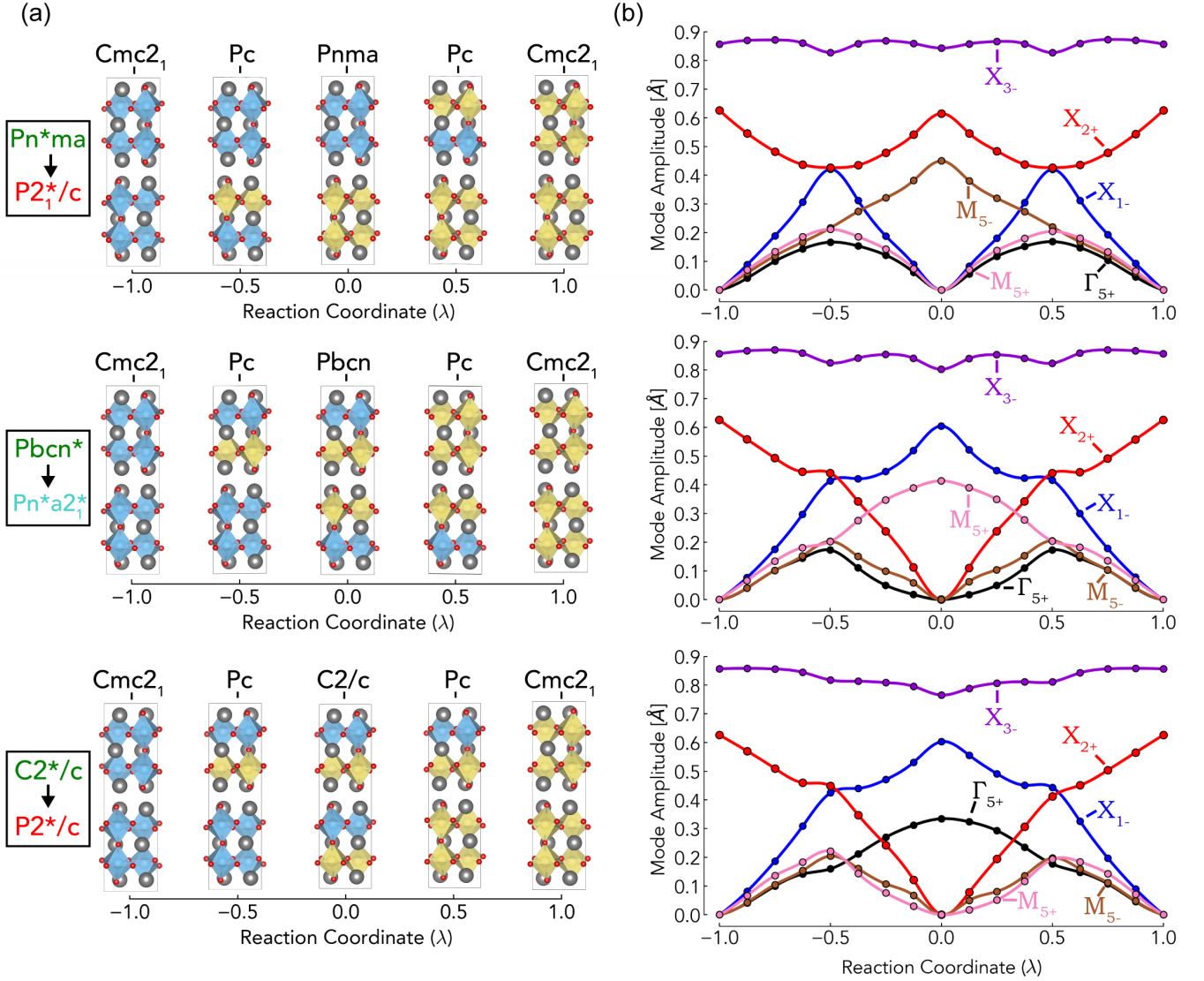
FIG. 4. Lowest energy four-step ferroelectric switching pathways obtained for $Ca_3Ti_2O_7$. (a) A visual illustration of one of the four-step paths from each pair in Figure 3(b) showing which sections of the perovskite slabs have transitioned from the initial to the final state. The spatial symmetry of each structure is shown above it. Labels of the distortion symmetry group of each path is shown on the left side with the symmetry of the parent two-step path above it. All six-four step paths involve the stepwise rotation of individual pairs of oxygen octahedra, with each one differing by the order in which all four pairs in the cell transition. (b) Amplitudes of modes of atomic displacements that transform as irreps of the high symmetry $I4/mmm$ structure of $Ca_3Ti_2O_7$ as a function of reaction coordinate for the paths shown in panel a. Structures at $\lambda = -0.5$ and $\lambda = 0.5$ for all six four-step paths show non-zero amplitudes of similar value that transform as the Γ_{5+}, M_{5+}, M_{5-}, X_{1-}, and X_{2+} irreps of $I4/mmm$. Differing structures at $\lambda = 0$ are then caused by different combinations of three of these decreasing to zero, with the remaining two increasing.

temperature magnetoelectric coupling[69]. It exhibits a large ferroelectric polarization, $\boldsymbol{P}$ ($\sim 100\,\mu C\,cm^{-2}$)[58] and a weak ferromagnetic moment, $\boldsymbol{M}$ ($\sim 0.1 - 1.0\ \mu_B/Fe$) arising from the canting of the antiferromagnetically aligned spins through an antisymmetric Dzyaloshinskii-Moriya (DM) interaction[70]. This system holds great promise for the *deterministic* control of the magnetization $\boldsymbol{M}$ using an electric field to control the polarization, $\boldsymbol{P}$, as recently reported in literature[13]. Should we expect a deterministic control of $\boldsymbol{M}$ with controlling $\boldsymbol{P}$? By systematically breaking the distortion symmetries associated with bulk ferroelectric switching in $BiFeO_3$, we discover two competing pathways that prevent such determinism. We also find that the symmetry breaking results in transient states with unconventional coupling between $\boldsymbol{M}$ and $\boldsymbol{P}$.
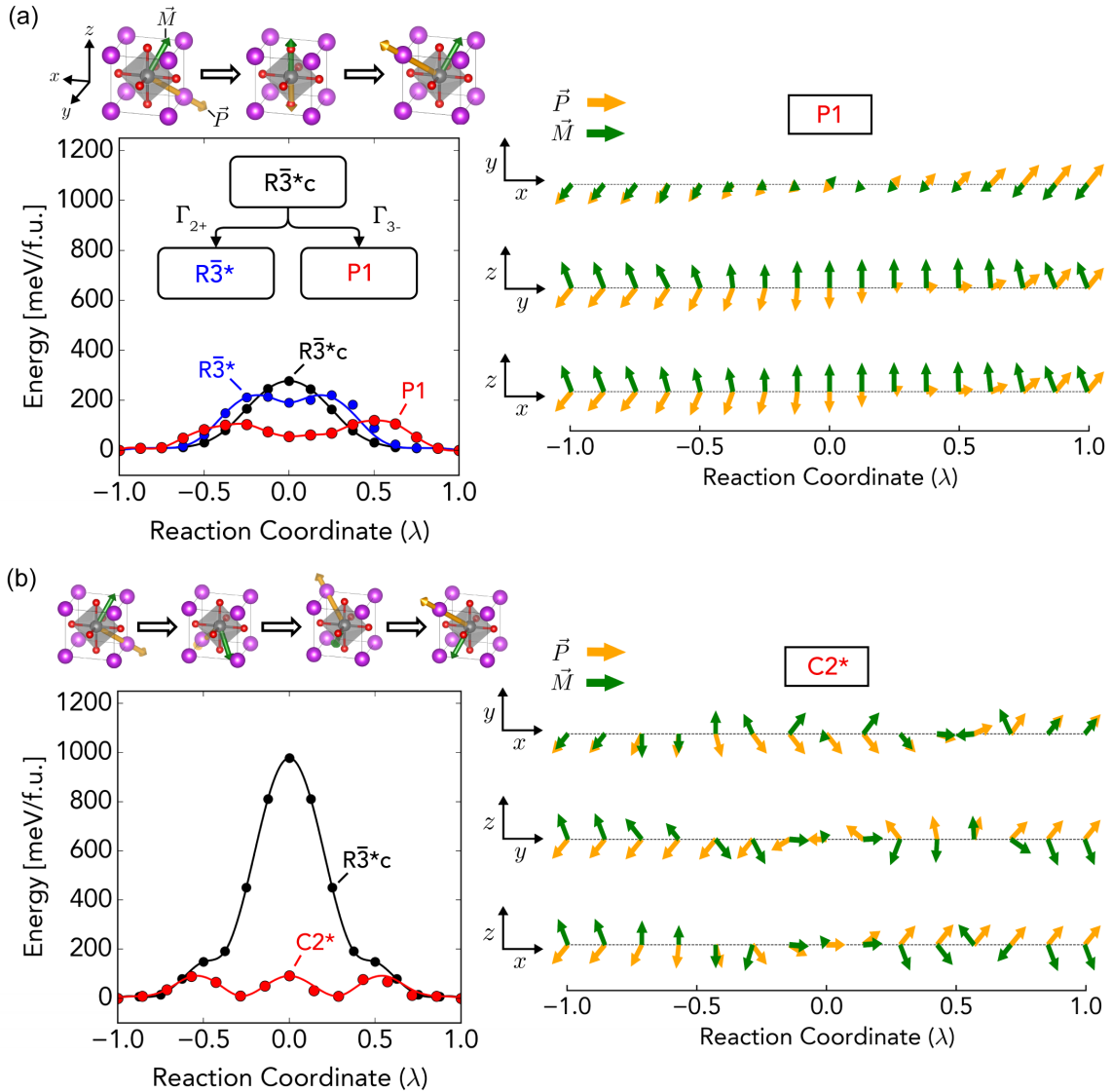
FIG. 5. Ferroelectric switching pathways in BiFeO$_3$ with and without the reversal of the net magnetization ($\boldsymbol{M}$). (a) Data for the switching pathway without reversal of the octahedral rotations where $\boldsymbol{P}$ is switched, and $\boldsymbol{M}$ is not. Shown on the left is the energy relative to the initial and final states from NEB calculations as a function of reaction coordinate for all of the paths obtained from perturbation of the initial path. Initial, middle, and final snapshots of $\boldsymbol{P}$ and $\boldsymbol{M}$ overlaid on a high-symmetry pseudocubic unit cell of BiFeO$_3$ is also displayed for the lowest energy $P1$ path. The purple, grey and red atoms represent Bi, Fe, and O respectively. Shown on the right are projections of $\boldsymbol{P}$ and $\boldsymbol{M}$ on various planes in the pseudocubic coordinate system for each image along the lowest energy path. (b) Data for the switching pathway with reversal of the octahedral rotations where both $\boldsymbol{P}$ and $\boldsymbol{M}$ are switched. Shown on the left is the energy relative to the initial and final states from NEB calculations as a function of reaction coordinate for all of the paths obtained from perturbation of the initial path. Snapshots of $\boldsymbol{P}$ and $\boldsymbol{M}$ overlaid on a high-symmetry pseudocubic unit cell of BiFeO$_3$ are also displayed for the four lowest energy images in the path. Shown on the right are projections of $\boldsymbol{P}$ and $\boldsymbol{M}$ on various planes in the pseudocubic coordinate system for each image along the lowest energy path.

To study this interaction, we start by considering two possible pathways to switch $\boldsymbol{P}$ - a nondeterministic path without octahedral rotations switching between the initial and final states (Figure 5a), and a deterministic path with such switching of octahedral rotations (Figure 5b). By doing so, we are able to specify whether $\boldsymbol{M}$ is also switched in the process, since a reversal of the oxygen octahedra necessitates a switching of the DM vector, and hence $\boldsymbol{M}$ as well[13]. For the path in panel a, only the polarization is reversed (nondeterministic), whereas for the path in panel b, the octahedral rotations and DM vector are both reversed (deterministic). Constructing

both paths using a linear interpolation between the end states shown in Supplementary Figure 2[27] results in path symmetries of $R\bar{3}^*c$. By performing NEB calculations, the black energy profiles shown in Figures 5(a) and 5(b) are produced. At this stage of exploration, additional NEB calculations can be performed after applying symmetry adapted perturbations constructed from the irreps of $R\bar{3}^*c$ shown in Supplementary Table 3[27]. What is ultimately obtained is a set of two paths with much lower overall energy barriers than the original, resulting from perturbations that transform as the Γ_{3-} irrep. It should be noted that in the case of the lowest energy path in panel b, the final path symmetry is $C2^*$ and not $P1$. While this is not the direct kernel of the irrep, it is one of its epikernels, and thus the NEB algorithm raising path symmetry to it is not surprising (see Supplementary Note 1 in Ref. 25). For the deterministic path in b, the MEP has an energy barrier of 90 meV/f.u. and consists of three 71° switching steps for $\boldsymbol{P}$ as it transitions from $[\bar{1}\bar{1}\bar{1}]_{ps}$ to $[111]_{ps}$, while passing through $[1\bar{1}\bar{1}]_{ps}$ and $[1\bar{1}1]_{ps}$. For the nondeterministic path in a, the energy barrier is 120 meV/f.u., and the resulting path exhibits two-step coordinated sequential motion of half of the Bi atoms and oxygen octahedra, producing the notable polarization and magnetization vectors along the path shown in Figure 5. In the first step of the nondeterministic path, half of the Bi atoms move along $[110]_{ps}$, while half of the octahedra rotate, causing all of them to be in phase about $[001]_{ps}$. In Glazer notation, this corresponds to a transition from an $a^-a^-a^-$ to $a^-a^-a^+$ structure. In the second half of the path, the octahedra return to their initial state, as all Bi atoms in the structure shift. This sequential motion of the A cations is of note, as recently this kind of behavior has been shown to lower bulk ferroelectric switching energies in corundum structured materials[71].

Thus, two distinct MEPs are presented for ferroelectric switching one which results in deterministic switching of $\boldsymbol{M}$ (90 meV/f.u.), and one that does not (120 meV/f.u.). With these pathways having comparable energy barriers, one would expect a competition between the two switching pathways at room temperature (300 K ∼ 25 meV). This is indeed what is observed experimentally (see supplementary data in Ref. 13), with switching proceeding through both pathways in strained thin films. Previous first-principles studies on strained BiFeO$_3$ have missed the latter path, resulting in an incomplete description of this process[13]. The fact that these pathways differ primarily in the behavior of the octahedral rotations indicates that strain could be used as a knob to energetically favor one pathway over the other, thus controlling the deterministic switching. Given the complex potential energy landscape associated with switching in transition metal oxide ferroelectrics, one would expect such competing pathways to be the norm rather than the exception. In this context, a systematic exploration of the switching pathways using distortion symmetry could provide a compelling platform to inform materials design.

In addition to the competing switching pathways, we discover that the nondeterministic switching pathway proceeds through the formation of a transient metastable state in which $\boldsymbol{P}$ and $\boldsymbol{M}$ and parallel to each other. This is noteworthy, since these order parameters usually assume mutually orthogonal directions in BiFeO$_3$. In general, the direction of $\boldsymbol{M}$ is restricted by the condition that its emergence through spin canting must not break the magnetic symmetry of the parent antiferromagnetic phase[72–76]. If this condition is satisfied, a structure with finite $\boldsymbol{M}$ may be stabilized through the DM antisymmetric exchange interaction. In the ground state of BiFeO$_3$, the polarization is in the $[111]_{ps}$ direction, and spins lie within the $(111)_{ps}$ plane in the parent antiferromagnetic structure, resulting in a magnetic space group symmetry of either Cc or Cc'. In both these cases, the only symmetry allowed direction for spin canting is within the $(111)_{ps}$ plane, so that $\boldsymbol{M}$ always remains perpendicular to $\boldsymbol{P}$. These results are consistent with previous work[70]. Note that this should also be true of all transient structures in the parent switching pathways with symmetry $R\bar{3}^*c$, and this is confirmed by our calculations (see supplementary material). However, for the intermediate metastable structure in the $P1$ nondeterministic switching pathway, the polarization is along $[001]_{ps}$, and the spins are oriented along $[1\bar{1}0]_{ps}$ in the parent antiferromagnetic structure, with a resultant magnetic space group symmetry of $Pn'a'2_1$. For this structure, $\boldsymbol{M} \parallel [001]_{ps}$ is the only symmetry allowed direction for canting. Finally, our non-collinear spin-polarized calculations show that this state exhibits a finite $\boldsymbol{M}$ along the $[001]_{ps}$ direction, indicating that this configuration with $\boldsymbol{M} \parallel \boldsymbol{P}$ is not only symmetry allowed, but is also stabilized by the DM interaction. The emergence of this unconventional transient state in our calculations is a direct consequence of systematic symmetry breaking of the switching pathways.

C. Application to domain wall motion in ferroelectric PbTiO$_3$

The third example of the DSM illustrates the possibility for exploration of the potential energy landscape by choosing an initial highly symmetrized path for the motion of a domain-wall in PbTiO$_3$ (Figure 6(a)).

180° ferroelectric domain-walls in PbTiO$_3$ have been studied extensively using a variety of first-principles techniques[77–83]. Although the PbTiO$_3$ supercell with Pb-centered domain walls used to construct the initial and final states in this study (Figure 6(a)) was relaxed, the true ground state structure was not initially obtained due to the constraining symmetry of the static structure. While this may result in paths with images that are lower in energy relative to the end points, it will be shown that this allows for an exploration of some of the neighboring energy landscape, and in turn, some of the many ways in which the different components of the polarization can behave during domain-wall motion.
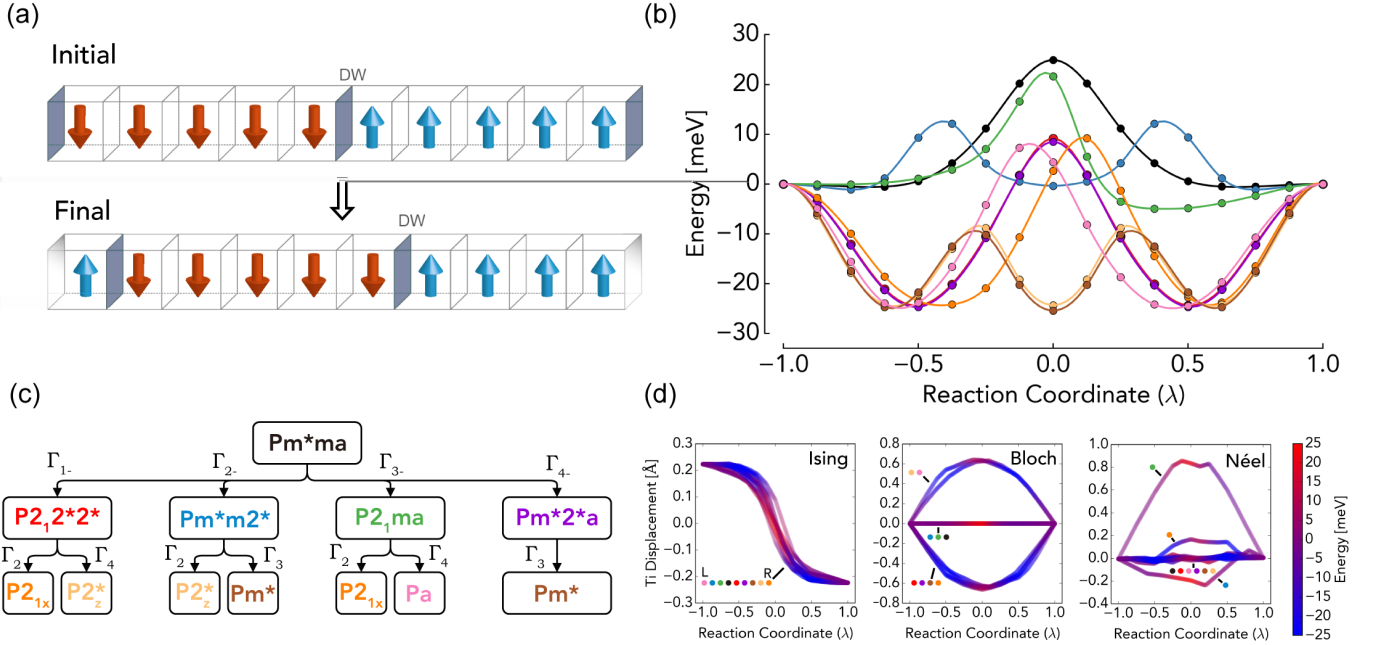
FIG. 6. Pathways obtained for $180°$ ferroelectric domain wall motion in PbTiO$_3$. (a) The structure of the supercells of the initial and final states used to construct the initial path for $180°$ domain-wall motion. Each box indicates a PbTiO$_3$ unit cell, with the red and blue arrows indicating polarization direction. (b) The energy relative to the initial and final states as a function of reaction coordinate for the final paths obtained from NEB calculations. The colors indicate the distortion group of the final path shown in the tree in panel c. (c) The tree of distortion symmetry groups resulting from path perturbations. (d) The Ising, Bloch, and Néel components of the Ti displacement for the first unit cell in the structures shown in panel a as a function of reaction coordinate. The energy of the complete structure is indicated by the color of the line, with the colored labels indicating which paths are present in the data.

First, an initial NEB calculation was carried out using the linearly interpolated path between the initial and final states. This has a path symmetry of Pm^*ma, and the resulting energy profile is shown in Figure 6(b). By constructing new initial paths for the NEB algorithm with symmetry-adapted perturbations, eight different final relaxed paths are obtained, as shown in Figures 6(b) and 6(c). By plotting the Ising, Bloch, and Néel components of the Ti displacement of one of the unit cells in the supercell through which the domain wall travels (i.e., the first cell in the structures in Figure 6(a)) as a function of reaction coordinate (λ), we can examine differences between the paths. The initial path shows the simultaneous movement of both walls in the supercell via a reduction of the Ising component of the polarization. For the Γ_{2-} path, the pathway consists of the same type of polarization behavior, but with a sequential movement of each wall. For the other paths obtained, Bloch and Néel components arise in the pathways, as shown in Figure 6(d). Although many of these paths share similar magnitudes of these, each path with a different symmetry exhibits different underlying atomic motion. The actual ground state structure and the MEP are close to the relaxed lowest energy structures and the path between them seen in Figure 6(b); see Supplementary Figure 7[27] for details.

Symmetry breaking at static ferroelectric domain walls is an important phenomena that has been shown to lead to a variety of novel properties localized about these regions. Some examples of these include an enhanced conductivity and photovoltaic effect[84–86]. Consequently, an understanding of the local structure of these interfaces is important, and has been a topic of great interest. Specific to PbTiO$_3$, previous work has illustrated an unexpected mixed Bloch-Néel-Ising character of static ferroelectric domain walls, similar to what can be observed at walls between magnetic domains[77,78]. In this work, we break symmetries associated with switching dynamics, and in turn, discover low energy pathways involving transient states that necessarily have non-zero Néel and Bloch components of the polarization as well. This result demonstrates how a selective breaking of distortion symmetry may be able to be used as a tool to help in the discovery of unique and previously inaccessible functional properties that may be intertwined with the dynamics of switching.

IV. CONCLUSION

In this work, we have illustrated a powerful new symmetry-based approach to discovering new MEPs which we call the distortion symmetry method (DSM).

By utilizing group theoretic tools, paths can be categorized according to their symmetry, and symmetry-adapted perturbations can be generated to allow this symmetry to be broken in a systematic manner. Using this approach within the NEB method, subsets of paths can be defined, each of which is explored for new MEPs. By applying this technique to a variety of systems involving bulk ferroelectric switching and domain-wall motion, new insights were gained. First, four-step bulk switching pathways were discovered for the improper ferroelectric $Ca_3Ti_2O_7$ with a large unit cell and a complex domain pattern. These provide new physical insights into the kinds of switching pathways that may be nucleated at experimentally observed domain walls in the material. Second, a new competing pathway was discovered for multiferroic switching in $BiFeO_3$ that allows for switching of polarization without switching canted magnetism. This low energy path exhibits parallel alignment of the net magnetization and polarization, and results in an indeterministic multiferroic switching process that competes with a deterministic path. This result informs studies where deterministic switching is sought[13]. Finally, a rich range of domain wall motion paths in the energy landscape of $PbTiO_3$ were discovered starting from a highly symmetrized initial path; walls with mixed Ising, Bloch, and Néel character were observed during the switching process. This demonstrates how breaking distortion symmetries may be able to be used to help probe unique functional properties associated with switching dynamics.

In order to complete calculations for the examples in the study, the distortion symmetry method was implemented to interface with standard NEB codes. This has resulted in an observed speedup of NEB calculations on paths containing starred symmetry of up to two times (see Supplementary Figures 9 and 10[27]). Furthermore, as demonstrated in this work, even in cases when the final MEP may have low symmetry, one can often start with a highly symmetrized initial pathway that allows the user to exploit the power of this method. In the future, we envision the possibility for further extensions to the distortion symmetry framework, by incorporating other kinds of symmetry groups, such as those involving distortion translation[87,88]. We foresee that the newly proposed distortion symmetry method could become an integral part of the discovery of new transition states in many problems of relevance to materials science.

* munrojm@psu.edu

[1] H. P. Hratchian and H. B. Schlegel, in *Theory and Applications of Computational Chemistry* (Elsevier, 2005) pp. 195–249.

[2] P. Pechukas, Annual Review of Physical Chemistry **32**, 159 (1981).

[3] R. G. Bone, Chemical Physics Letters **193**, 557 (1992).

[4] J. W. McIver and R. E. Stanton, Journal of the American Chemical Society **94**, 8618 (1972).

[5] H. L. Zhuang, M. D. Johannes, A. K. Singh, and R. G. Hennig, Physical Review B **96**, 165305 (2017).

[6] K. Wang, J. Chen, X. Zhang, and W. Zhu, Journal of Applied Physics **122**, 105107 (2017).

[7] P. Lu, J.-S. Kim, J. Yang, H. Gao, J. Wu, D. Shao, B. Li, D. Zhou, J. Sun, D. Akinwande, D. Xing, and J.-F. Lin, Physical Review B **94**, 224512 (2016).

[8] S. L. Shang, L. G. Hector, Y. Wang, and Z. K. Liu, Physical Review B **83**, 224104 (2011).

[9] H. Z. Fang, S. L. Shang, Y. Wang, Z. K. Liu, D. Alfonso, D. E. Alman, Y. K. Shin, C. Y. Zou, A. C. T. van Duin, Y. K. Lei, and G. F. Wang, Journal of Applied Physics **115**, 043501 (2014).

[10] T. D. Huan, V. Sharma, G. a. Rossetti, and R. Ramprasad, Physical Review B - Condensed Matter and Materials Physics **90**, 1 (2014).

[11] B. J. Demaske, A. Chernatynskiy, and S. R. Phillpot, Journal of Physics: Condensed Matter **28**, 165901 (2016).

[12] J. W. Bennett, K. F. Garrity, K. M. Rabe, and D. Vanderbilt, Physical Review Letters **110**, 017603 (2013).

[13] J. T. Heron, J. L. Bosse, Q. He, Y. Gao, M. Trassin, L. Ye, J. D. Clarkson, C. Wang, J. Liu, S. Salahuddin, D. C. Ralph, D. G. Schlom, J. Íñiguez, B. D. Huey, and R. Ramesh, Nature **516**, 370 (2014).

[14] E. a. Nowadnick and C. J. Fennie, Physical Review B **94**, 104105 (2016).

[15] T. Vegge, T. Rasmussen, T. Leffers, O. B. Pedersen, and K. W. Jacobsen, Physical Review Letters **85**, 3866 (2000).

[16] S. Shang, W. Wang, B. Zhou, Y. Wang, K. Darling, L. Kecskes, S. Mathaudhu, and Z. Liu, Acta Materialia **67**, 168 (2014).

[17] Y. Kumagai and N. A. Spaldin, Nature Communications **4**, 1540 (2013).

[18] A. Chandrasekaran, D. Damjanovic, N. Setter, and N. Marzari, Physical Review B - Condensed Matter and

Materials Physics **88**, 1 (2013).

[19] P. Tao, M. Hodošček, J. D. Larkin, Y. Shao, and B. R. Brooks, Journal of Chemical Theory and Computation **8**, 5035 (2012).

[20] H. Jónsson, G. Mills, and K. W. Jacobsen, in *Classical and Quantum Dynamics in Condensed Phase Simulations* (World Scientific, 1998) pp. 385–404.

[21] R. a. Olsen, G. J. Kroes, G. Henkelman, a. Arnaldsson, and H. Jónsson, Journal of Chemical Physics **121**, 9776 (2004).

[22] P. M. Zimmerman, Journal of Computational Chemistry **34**, 1385 (2013).

[23] H. B. Schlegel, Wiley Interdisciplinary Reviews: Computational Molecular Science **1**, 790 (2011).

[24] M. Jafari and P. M. Zimmerman, Journal of Computational Chemistry **38**, 645 (2017).

[25] B. K. VanLeeuwen and V. Gopalan, Nature Communications **6**, 8818 (2015).

[26] B. K. VanLeeuwen, V. Gopalan, and D. B. Litvin, Acta Crystallographica Section A: Foundations and Advances **70**, 24 (2014).

[27] See Supplemental Material at [URL will be inserted by publisher] for additional information regarding the presented data and method implementation, as well as POSCAR formatted files for the images in all of the reported paths.

[28] A. Goodrow, A. T. Bell, and M. Head-Gordon, Journal of Chemical Physics **129** (2008).

[29] G. Henkelman, Annual Review of Materials Research **47**, annurev (2017).

[30] C. Dellago, P. G. Bolhuis, and D. Chandler, Journal of Chemical Physics **110**, 6617 (1999).

[31] C. Dellago, P. G. Bolhuis, and P. L. Geissler, Computer Simulations in Condensed Matter Systems: From Materials to Chemical Biology **l**, 1 (2006).

[32] P. G. Bolhuis, D. Chandler, C. Dellago, and P. L. Geissler, Annual Review of Physical Chemistry **53**, 291 (2002).

[33] X.-J. Zhang and Z.-P. Liu, Phys. Chem. Chem. Phys. **17**, 2757 (2015).

[34] A. Banerjee, N. Adams, J. Simons, and R. Shepard, Journal of Physical Chemistry **89**, 52 (1985).

[35] J. Baker, Journal of Computational Chemistry **7**, 385 (1986).

[36] C. J. Cerjan and W. H. Miller, The Journal of Chemical Physics **75**, 2800 (1981).

[37] A. Cammarata and T. Polcar, Physical Review B **96**, 1 (2017).

[38] D. J. Wales, Molecular Physics **100**, 3285 (2002).

[39] D. J. Wales, International Reviews in Physical Chemistry **25**, 237 (2006).

[40] S. Liu, I. Grinberg, and A. M. Rappe, Nature **534**, 360 (2016).

[41] G. Kresse and J. Hafner, Physical Review B **47**, 558 (1993).

[42] G. Kresse and J. Furthmüller, Computational Materials Science **6**, 15 (1996).

[43] G. Kresse and J. Furthmüller, Physical Review B **54**, 11169 (1996).

[44] G. Kresse and D. Joubert, Physical Review B **59**, 1758 (1999).

[45] P. Giannozzi, S. Baroni, N. Bonini, M. Calandra, R. Car, C. Cavazzoni, D. Ceresoli, G. L. Chiarotti, M. Cococcioni, I. Dabo, A. Dal Corso, S. de Gironcoli, S. Fabris, G. Fratesi, R. Gebauer, U. Gerstmann, C. Gougoussis, A. Kokalj, M. Lazzeri, L. Martin-Samos, N. Marzari,

F. Mauri, R. Mazzarello, S. Paolini, A. Pasquarello, L. Paulatto, C. Sbraccia, S. Scandolo, G. Sclauzero, A. P. Seitsonen, A. Smogunov, P. Umari, and R. M. Wentzcovitch, Journal of Physics: Condensed Matter **21**, 395502 (2009).

[46] K. Momma and F. Izumi, Journal of Applied Crystallography **41**, 653 (2008).

[47] C. J. Bradley and A. P. Cracknell, *The Mathematical Theory of Symmetry in Solids* (Oxford University Press, 2010).

[48] A. Togo, "Spglib," (2009).

[49] H. T. Stokes, B. J. Campbell, and R. Cordes, Acta Crystallographica Section A Foundations of Crystallography **69**, 388 (2013).

[50] J. P. Perdew, A. Ruzsinszky, G. I. Csonka, O. A. Vydrov, G. E. Scuseria, L. A. Constantin, X. Zhou, and K. Burke, Physical Review Letters **100**, 136406 (2008).

[51] C. F. Li, S. H. Zheng, H. W. Wang, J. J. Gong, X. Li, Y. Zhang, K. L. Yang, L. Lin, Z. B. Yan, S. Dong, and J.-M. Liu, Physical Review B **97**, 184105 (2018).

[52] M. Methfessel and A. T. Paxton, Physical Review B **40**, 3616 (1989).

[53] D. Sheppard, P. Xiao, W. Chemelewski, D. D. Johnson, and G. Henkelman, The Journal of Chemical Physics **136**, 074103 (2012).

[54] V. I. Anisimov, Journal of Physics: Condensed Matter **9**, 767 (1997).

[55] S. Dudarev and G. Botton, Physical Review B - Condensed Matter and Materials Physics **57**, 1505 (1998).

[56] H. Wang, Y. Zheng, M. Q. Cai, H. Huang, and H. L. Chan, Solid State Communications **149**, 641 (2009).

[57] S. L. Shang, G. Sheng, Y. Wang, L. Q. Chen, and Z. K. Liu, Physical Review B - Condensed Matter and Materials Physics **80**, 1 (2009).

[58] S. Picozzi and C. Ederer, Journal of Physics Condensed Matter **21**, 1 (2009).

[59] J. K. Shenton, D. R. Bowler, and W. L. Cheah, Journal of Physics: Condensed Matter **29**, 445501 (2017).

[60] P. E. Blöchl, O. Jepsen, and O. K. Andersen, Physical Review B **49**, 16223 (1994).

[61] M. F. Taib, M. K. Yaakob, O. H. Hassan, and M. Z. Yahya, Integrated Ferroelectrics **142**, 119 (2013).

[62] N. A. Benedek and C. J. Fennie, Physical Review Letters **106**, 107204 (2011).

[63] A. B. Harris, Physical Review B **84**, 064116 (2011).

[64] F. T. Huang, F. Xue, B. Gao, L. H. Wang, X. Luo, W. Cai, X. Z. Lu, J. M. Rondinelli, L. Q. Chen, and S. W. Cheong, Nature Communications **7**, 11602 (2016).

[65] F. T. Huang, B. Gao, J. W. Kim, X. Luo, Y. Wang, M. W. Chu, C. K. Chang, H. S. Sheu, and S. W. Cheong, arXiv **1**, 1 (2016).

[66] S. M. Park, B. Wang, S. Das, S. C. Chae, J. S. Chung, J. G. Yoon, L. Q. Chen, S. M. Yang, and T. W. Noh, Nature Nanotechnology , 1 (2018).

[67] R. Xu, S. Liu, I. Grinberg, J. Karthik, A. R. Damodaran, A. M. Rappe, and L. W. Martin, Nature Materials **14**, 79 (2015).

[68] X. Z. Lu and J. M. Rondinelli, Nature Materials **15**, 951 (2016).

[69] J.-C. Yang, Q. He, P. Yu, and Y.-H. Chu, Annual Review of Materials Research **45**, 249 (2015).

[70] C. Ederer and N. A. Spaldin, Physical Review B **71**, 060401 (2005).

[71] M. Ye and D. Vanderbilt, Physical Review B **93**, 1 (2016).

[72] I. E. Dzialoshinskii, Soviet Physics **5**, 1259 (1957).

[73] I. Dzyaloshinsky, Journal of Physics and Chemistry of Solids **4**, 241 (1958).

[74] T. Moriya, Phys. Rev. Lett. **4**, 228 (1960).

[75] T. Moriya, Physical Review **120**, 91 (1960).

[76] C. J. Fennie, Physical Review Letters **100**, 1 (2008).

[77] D. Lee, R. K. Behera, P. Wu, H. Xu, Y. L. Li, S. B. Sinnott, S. R. Phillpot, L. Q. Chen, and V. Gopalan, Physical Review B **80**, 060102 (2009).

[78] R. K. Behera, C.-W. Lee, D. Lee, A. N. Morozovska, S. B. Sinnott, A. Asthagiri, V. Gopalan, and S. R. Phillpot, Journal of Physics: Condensed Matter **23**, 175902 (2011).

[79] X. Wang, S. Tomoda, T. Shimada, and T. Kitamura, Physica B: Condensed Matter **410**, 22 (2013).

[80] J. C. Wojde and J. Íñiguez, Physical Review Letters **112**, 247603 (2014).

[81] Y. J. Wang, D. Chen, Y. L. Tang, Y. L. Zhu, and X. L. Ma, Journal of Applied Physics **116**, 224105 (2014).

[82] B. Meyer and D. Vanderbilt, Physical Review B **65**, 104111 (2002).

[83] L. He and D. Vanderbilt, Physical Review B **68**, 134103 (2003).

[84] J. Seidel, L. W. Martin, Q. He, Q. Zhan, Y. H. Chu, A. Rother, M. E. Hawkridge, P. Maksymovych, P. Yu, M. Gajek, N. Balke, S. V. Kalinin, S. Gemming, F. Wang, G. Catalan, J. F. Scott, N. a. Spaldin, J. Orenstein, and R. Ramesh, Nature Materials **8**, 229 (2009).

[85] S. Y. Yang, J. Seidel, S. J. Byrnes, P. Shafer, C. H. Yang, M. D. Rossell, P. Yu, Y. H. Chu, J. F. Scott, J. W. Ager, L. W. Martin, and R. Ramesh, Nature Nanotechnology **5**, 143 (2010).

[86] P. Zubko, S. Gariglio, M. Gabay, P. Ghosez, and J.-M. Triscone, Annual Review of Condensed Matter Physics **2**, 141 (2011).

[87] H. Padmanabhan, M. L. Kingsland, J. M. Munro, D. B. Litvin, and V. Gopalan, Symmetry **9**, 1 (2017).

[88] V. S. Liu, B. K. VanLeeuwen, J. M. Munro, H. Padmanabhan, I. Dabo, V. Gopalan, and D. B. Litvin, Acta Crystallographica Section A Foundations and Advances **74**, 4 (2018).